J. Fluid Mech. (2025), *vol.* 1006, A13, doi:10.1017/jfm.2025.114

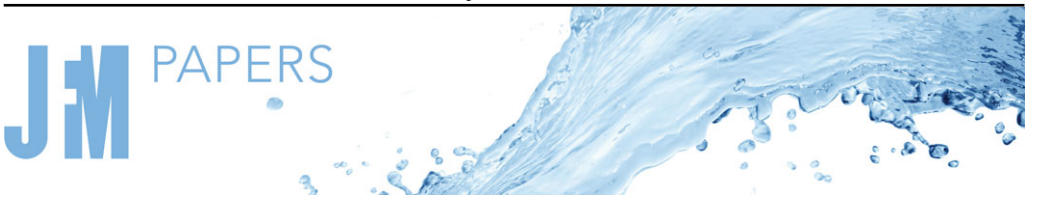

Instability in centrifugally stable shear flows

Kengo Deguchi[1] **and Ming Dong**[2]

[1]School of Mathematics, Monash University, Clayton, VIC 3800, Australia

[2]State Key Laboratory of Nonlinear Mechanics, Chinese Academy of Sciences, Institute of Mechanics, Beijing 100190, PR China

Corresponding authors: Kengo Deguchi, kengo.deguchi@monash.edu; Ming Dong, dongming@imech.ac.cn

(Received 3 October 2024; revised 9 December 2024; accepted 18 January 2025)

We investigate the linear instability of flows that are stable according to Rayleigh's criterion for rotating fluids. Using Taylor–Couette flow as a primary test case, we develop large-Reynolds-number-matched asymptotic expansion theories. Our theoretical results not only aid in detecting instabilities previously reported by Deguchi (*Phys. Rev. E,* vol 95, 2017, p. 021102(R)) across a wide parameter range, but also clarify the physical mechanisms behind this counterintuitive phenomenon. Instability arises from the interaction between large-scale inviscid vortices and the viscous flow structure near the wall, which is analogous to Tollmien–Schlichting waves. Furthermore, our asymptotic theories and numerical computations reveal that similar instability mechanisms occur in boundary layer flows over convex walls.

Key words: high-speed flow, Taylor-Couette flow, critical layers

1. Introduction

Flows deemed unstable by Rayleigh's stability criterion of rotating fluid flows (Rayleigh 1917) are often simply referred to as centrifugally unstable flows. Taylor–Görtler vortices are textbook examples of flows generated by such instabilities (e.g. Drazin & Reid 1981).

The derivation of the Rayleigh criterion relies on two assumptions: axisymmetry and the inviscid nature of the flow. However, the criterion is known to reasonably align with Navier–Stokes-based stability analyses for general perturbations. An illustrative example comes from the stability analysis of Taylor–Couette flow, where the Reynolds numbers R_i and R_o pertain to the rotation speeds of the inner and outer cylinders, respectively. In the R_o–R_i parameter plane shown in figure 1, the shaded region becomes stable according

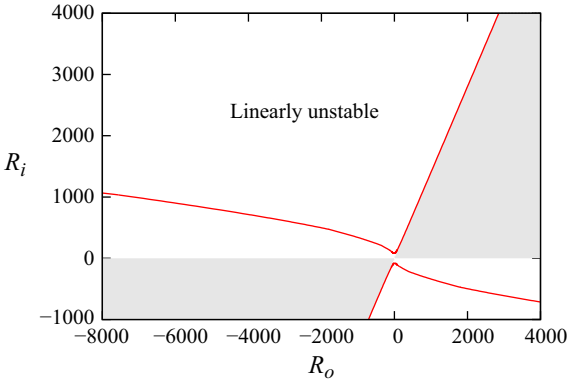

Figure 1. Stability of Taylor–Couette flow for the radius ratio $\eta = 5/7$. The red curve is the neutral curve. When the cylinders are co-rotating ($R_i R_o > 0$), the most unstable modes are axisymmetric. In contrast, for the counter-rotating case ($R_i R_o < 0$), the majority of the neutral curve is determined by non-axisymmetric modes. The shaded region is stable according to the Rayleigh's stability criterion, and bounded by the Rayleigh line $R_i = R_o/\eta$ and $R_i = 0$.

to the Rayleigh criterion. One of the boundaries of this region, known as the Rayleigh line, accurately predicts the onset of Taylor vortices at large enough rotation rates (Taylor 1923; Lewis 1928). The other boundary corresponds to the case where the inner cylinder is fixed and the outer cylinder is rotated. In Drazin & Reid (1981), this flow is introduced as an example of a flow that is always linearly stable, along with plane Couette flow and Hagen–Poiseuille flow.

Near the latter $R_i = 0$ line, non-axisymmetric disturbances, for which the Rayleigh criterion cannot account, become most unstable. Nevertheless, subsequent physical scaling arguments (Esser & Grossman 1996), detailed numerical eigenvalue analysis (Meseguer 2002), and asymptotic theory (Deguchi 2016) all agreed on the conclusion that this type of linear instability cannot extend into the Rayleigh stable parameter region, supporting the belief that diffusion and/or non-axisymmetry act as stabilising mechanisms.

It was therefore widely unexpected when Deguchi (2017) numerically found linear instability across the $R_i = 0$ line; following Ayats *et al.* (2020), we refer to this mode as the D17 mode. This mode, also characterised by its non-axisymmetric nature, appears at very high Reynolds numbers, making numerical computations challenging. Although the instability in the centrifugally stable regime has indeed been detected by multiple independent numerical codes, there are still some opinions questioning its existence, as the underlying physical mechanism remains elusive. The primal aim of this paper is to establish beyond doubt the origin of the D17 mode. Our idea is to employ the matched asymptotic expansion analysis, which has a long history of elucidating various shear flow instabilities. In this approach, the largeness of the Reynolds number is rather a favourable effect for constructing mathematically rational approximate solutions and clarifying the physical instability mechanism.

Not much is known about the properties of the D17 mode, but one notable characteristic is its longer wavelength compared with classical instabilities in Taylor–Couette flow. The mode therefore disregards the short-wavelength-type stability criteria (Billant & Gallaire 2005; Kirillov & Mutabazi 2017), which apply to non-axisymmetric disturbances. Deguchi (2017) speculated on possible similarities between the D17 mode with Tollmien–Schlichting (TS) waves because they both appear in inviscidly stable shear flows and have long wavelengths. Brockmann *et al.* (2023) recently analysed spiral Poiseuille flow and

reported that the TS wave instability evolves continuously into the D17 modes. However, while TS waves usually exhibit longer wavelengths with increasing Reynolds numbers, the wavelength of the D17 mode in Taylor–Couette flow remains nearly constant. Furthermore, even in parallel flows where linear instability does not occur, the D17 mode can still manifest by incorporating Rayleigh-stable effects. This is evident in the narrow-gap limit of Taylor–Couette flow where the governing equations closely resemble those for plane Couette flow. The above numerical facts indicate that directly applying the well-known TS wave asymptotic theory developed by Tollmien (1929); Schlichting (1933) and Lin (1955) to the D17 mode is not possible.

If the new asymptotic theory for Taylor–Couette flow proves successful, it could also serve as a guide to demonstrate the existence of similar instabilities in other, more practically significant flows. Of particular interest is the boundary layer flow over a curved wall. The Görtler vortex, which occurs when the wall surface is concave, has been intensively studied by many researchers (Görtler 1941; Hall 1982, 1983, 1988; Saric 1994). While, when the wall is convex, Floryan (1986) showed that the flow is inviscidly stable applying Raylegh's theorem. Moreover, local stability analysis based on the Orr–Sommerfeld equation has traditionally indicated no instability in this scenario, thus limiting detailed examination. The recent work by Karp & Hack (2018) therefore sought a transition route to turbulence that does not rely on linear modal instabilities of the basic flow. Their research is motivated by experiments of boundary layer flows over a wall with convex and concave regions (e.g. Kalburgi *et al.* 1988; Benmalek & Saric 1994). However, to the best of the authors' knowledge, there are no detailed experimental studies focusing exclusively on convex surfaces.

The rest of the paper is structured as follows. In § 2, we study the narrow-gap limit of Taylor–Couette flow. In this limit, the eigenvalue problem governing stability is greatly simplified, making it ideal for presenting the essence of the asymptotic structure. Our analysis will reveal both similarities and differences between the TS and D17 modes. Section 3 extends the theoretical results to fully wide-gap Taylor–Couette flow. In § 4, we demonstrate that a similar theory can be applied to boundary layer flow over a convex wall. Finally, in § 5, we draw some conclusions.

2. Narrow-gap Taylor–Couette flow

2.1. *Formulation of the problem*

Consider incompressible fluid flow with kinematic viscosity ν between two co-axial cylinders of dimensional inner and outer radii r_i^* and r_o^*. We choose the cylinder gap, $d^* = r_o^* - r_i^*$, as the length scale. The arrangement of the cylinders is hence uniquely determined by the radius ratio $\eta = r_i^*/r_o^* \leqslant 1$. The diffusive time scale, $(d^*)^2/\nu$, is the conventional choice for describing Taylor–Couette flow. Using the associated velocity scale, ν/d^*, and the pressure scale, $\rho^*\nu^2/(d^*)^2$, where ρ^* is the fluid density, the dimensionless velocity $\mathbf{v}$ and pressure p fields are governed by the Navier–Stokes equations

$$\partial_t \mathbf{v} + (\mathbf{v}\cdot\nabla)\mathbf{v} = -\nabla p + \nabla^2\mathbf{v} \tag{2.1}$$

and the divergence-free condition $\nabla\cdot\mathbf{v} = 0$. Due to the use of the viscous scale, the Reynolds number does not appear in the diffusion terms. Instead, the normalised angular velocities of the cylinders define the two conventional Reynolds numbers. In non-dimensional cylindrical coordinates (r, θ, z), the no-slip boundary conditions at the

cylinder walls are prescribed as

$$\mathbf{v}(r_i, \theta, z) = (0, R_i, 0), \quad \mathbf{v}(r_o, \theta, z) = (0, R_o, 0), \tag{2.2}$$

where $r_i = \eta/(1-\eta)$ and $r_o = 1/(1-\eta)$. The Reynolds numbers and the dimensional angular velocities of the inner and outer cylinders, Ω_i^* and Ω_o^*, are related through

$$R_i = \frac{\Omega_i^* r_i^* d^*}{\nu}, \qquad R_o = \frac{\Omega_o^* r_o^* d^*}{\nu}. \tag{2.3}$$

As is well known, the laminar circular Couette solution can be written as $(u, v, w, p) = (0, R_o\, r\Omega(r), 0, R_o^2 \int^r r_* \Omega^2(r_*) \mathrm{d}r_*)$, where the scaled angular velocity has the analytic form

$$\Omega(r) = A + B/r^2 \tag{2.4}$$

with the constants

$$A \equiv \frac{1-\eta^2 a}{1+\eta}, \qquad B \equiv \frac{a-1}{1+\eta} r_i^2, \qquad a \equiv \frac{R_i}{\eta R_o}. \tag{2.5}$$

The Rayleigh line corresponds to $a = \eta^{-2}$. The Rayleigh stable region is thus written as $a \in [0, \eta^{-2}]$, and it includes the solid-body rotation $a = 1$.

2.2. *Narrow-gap limit*

Now we derive the reduced problem valid at the narrow-gap limit $\eta \to 1$. We introduce a small perturbation parameter $\delta = \sqrt{1-\eta}$ and expand

$$(u, v, w, p) = (u^+, \delta^{-1} v^+, w^+, p^+) + \cdots, \quad (R_o, R_i) = \delta^{-1}(Re, aRe) + \cdots. \tag{2.6}$$

Changing the coordinates as $y = r - r_i$, $x = \delta^{-1}\theta$ and only retaining the leading-order terms, we get

$$(\partial_t + v^+\partial_x + u^+\partial_y + w^+\partial_z)u^+ - v^{+2} = -p_y^+ + (\partial_y^2 + \partial_z^2)u^+, \tag{2.7a}$$

$$(\partial_t + v^+\partial_x + u^+\partial_y + w^+\partial_z)v^+ = (\partial_y^2 + \partial_z^2)v^+, \tag{2.7b}$$

$$(\partial_t + v^+\partial_x + u^+\partial_y + w^+\partial_z)w^+ = -p_z^+ + (\partial_y^2 + \partial_z^2)w^+, \tag{2.7c}$$

$$\partial_x v^+ + \partial_y u^+ + \partial_z w^+ = 0, \tag{2.7d}$$

and the boundary conditions

$$(u^+, v^+, w^+) = (0, Re, 0) \qquad \text{at} \qquad y = 1, \tag{2.8a}$$

$$(u^+, v^+, w^+) = (0, aRe, 0) \qquad \text{at} \qquad y = 0. \tag{2.8b}$$

The limiting process here is essentially that used by Hall (1982, 1983, 1988) for the Görtler vortex problem, and the final set of equations is often referred to as the boundary region equations. The laminar circular Couette flow now becomes a linear profile

$$(u^+, v^+, w^+, p^+) = (0, Re\, v_b(y), 0, Re^2 p_b(y)), \qquad v_b(y) = (1-a)y + a. \tag{2.9}$$

The last term on the left-hand side of (2.7*a*) is the Görtler term, representing the deviation from the plane Couette problem.

Stability of the basic flow to infinitesimal perturbations can be analysed by writing

$$(u^+, v^+, w^+, p^+) = (0, Re\, v_b(y), 0, Re^2 p_b(y)) + (\hat{u}(y), \hat{v}(y), \hat{w}(y), Re\, \hat{p}(y)) \exp(i\alpha(x - Re\, ct) + ikz) + \text{c.c.} \quad (2.10)$$

and linearising (2.7). Here, c.c. denotes the complex conjugate. To ease notation, we shall drop the hats after substitution. Eliminating the pressure and the axial velocity component, we arrive at the coupled equations

$$\mathcal{L}v + v_b' u = 0, \qquad \mathcal{L}(u'' - k^2 u) + 2v_b k^2 v = 0, \quad (2.11)$$

involving the linear operator $\mathcal{L} = i\alpha(v_b - c) - Re^{-1}(\partial_y^2 - k^2)$. The prime denotes differentiation with respect to y. The above equations and the boundary conditions $u = u' = v = 0$ imposed at $y = 0$ and 1 constitute an eigenvalue problem for the complex growth rate $c = c_r + ic_i$. From the symmetry of the system, it is sufficient to consider positive scaled azimuthal wavenumber α and axial wavenumber k. The flow is unstable if $c_i > 0$.

The following mathematical facts are immediately apparent.

(i) Squire's theorem does not hold due to the presence of the Görtler term.

(ii) If $k = 0$, the stability problem is equivalent to that for plane Couette flow. Therefore, the well-known proof by Romanov (1973) can be applied, showing that no instability exists.

(iii) The parameter range $a \in [0, 1]$ corresponds to the Rayleigh stable case. In this regime, the flow is stable if $\alpha = 0$, i.e. the flow is axisymmetric. As remarked in § 1, the Rayleigh criterion assumes the flow to be inviscid. However, even if we include the viscous terms, we can still show the absence of instability, as the proof by Synge (1938) for Taylor–Couette flow is still valid for the narrow-gap limit equations.

It follows that for the Rayleigh stable case $a \in [0, 1]$, instability is impossible if either α or k is zero.

In the rest of § 2, we focus on the stationary inner cylinder case $a = 0$ for simplicity. The eigenvalue problem (2.11) can be numerically solved by the Chebyshev collocation method. With increasing Re from zero, an instability emerges at $(Re, \alpha, k) = (2.831 \times 10^7, 0.978, 1.350)$, as reported by Deguchi (2017); see figure 2. Like many other shear flows, the size of the instability region in the wavenumber plane expands as the Reynolds number increases further. However, in the current eigenvalue problem, the flow becomes unstable only within a very narrow region, making detection of this instability through numerical computations extremely difficult.

Figure 3(*a*) shows the neutral curve for $\alpha = 0.978$, with the corresponding phase speed depicted in figure 3(*b*). The two branches of the neutral curve emanating from the aforementioned critical point exhibit large-Reynolds-number asymptotic characteristics somewhat similar to TS waves. Indeed, we shall see in §§ 2.3 and 2.4 that the asymptotic structure of the perturbation near the wall bears similarities to that studied by Tollmien (1929); Schlichting (1933) and Lin (1945, 1955). For this reason, we adopt the terms upper and lower branches in figure 2 so that they preserve this analogy. The red dashed curves in the figures are the asymptotic results to be derived in §§ 2.3 and 2.4. For the lower branch, a reasonably accurate asymptotic approximation is obtained for a fairly wide range of Re. In contrast, the upper branch exhibits a wiggle, and only beyond this point does the asymptotic result provide a good approximation. These features were also observed in neutral curves of TS waves in channel flows and boundary layer flows (see Drazin & Reid (1981), for example).

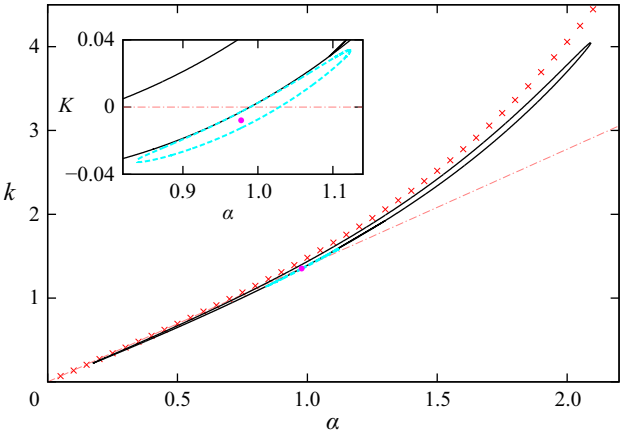

Figure 2. Linear instability found in the narrow-gap Taylor–Couette flow problem (2.11) for the stationary inner cylinder case $a = 0$.The magenta bullet indicate the wavenumber pair $(\alpha, k) = (0.978, 1.350)$ at which the instability first emerges at $Re = 2.831 \times 10^7$. The cyan dashed and black solid curves are the neutral curves for $Re = 2.9 \times 10^7$ and 10^8, respectively. The crosses are found by the large-Re asymptotic result (2.16). The dash-dotted line is $k = (5\pi/8\sqrt{2})\alpha$ found by the analysis of the Kummer's function. In the inset, $K = k - (5\pi/8\sqrt{2})\alpha$ is used to illustrate the structure of the unstable regions clearly.

The phase velocity c provides important insight into the structure of the eigenfunctions because a thin vortex layer, known as the critical layer, typically forms around the region where the base flow speed matches c. The magnitude of c drops with increasing Re, as seen in figure 3(b), suggesting that if there is a critical layer, it should be sitting around $y = 0$, where the base-flow velocity is small. The radial eigenfunction u for the lower branch, shown in figure 4, indicates that there is indeed some structure near the inner cylinder, while the perturbation does not diminish in the core region away from the wall surface. The nature of the interaction between the core flow and the near-wall layer will naturally be revealed by the method of matched asymptotic expansion. Our theory will also demonstrate that constant wavelengths are necessary to maintain the core structure. Thus, as seen in figure 3(a), the wavenumber does not decrease with increasing Re, unlike TS waves.

2.3. *Lower branch asymptotic analysis*

Let us start by analysing the lower branch, which has a relatively simple asymptotic structure. We fix α at a positive constant throughout the analysis. When Re is asymptotically large, the majority of the fluid layer is occupied by an inviscid core region, while near the inner cylinder ($y = 0$), a thin viscous wall layer of thickness $O(\epsilon)$ emerges (see figure 5a). Since we have set $a = 0$, within the boundary layer, the size of v_b is $O(\epsilon)$. Therefore, the advective effect of $O(\epsilon)$ and the viscous effect of $O(Re^{-1}\epsilon^{-2})$ in the operator $\mathcal{L}$ in (2.11) balance when $\epsilon = Re^{-1/3}$. This wall layer thickness is typical of critical layers, where the phase speed of the wave matches the base flow speed.

Using the small parameter ϵ, we expand $k = k_0 + \epsilon k_1 + \cdots$ and $c = \epsilon c_1 + \cdots$. The overall structure of the asymptotic problem is as follows. First, the leading-order inviscid core problem determines k_0. Then, at the next order, the core flow is coupled with the wall layer problem to yield the dispersion relation linking c_1 and k_1. In the neutral case, c_1 and k_1 can be solved explicitly.

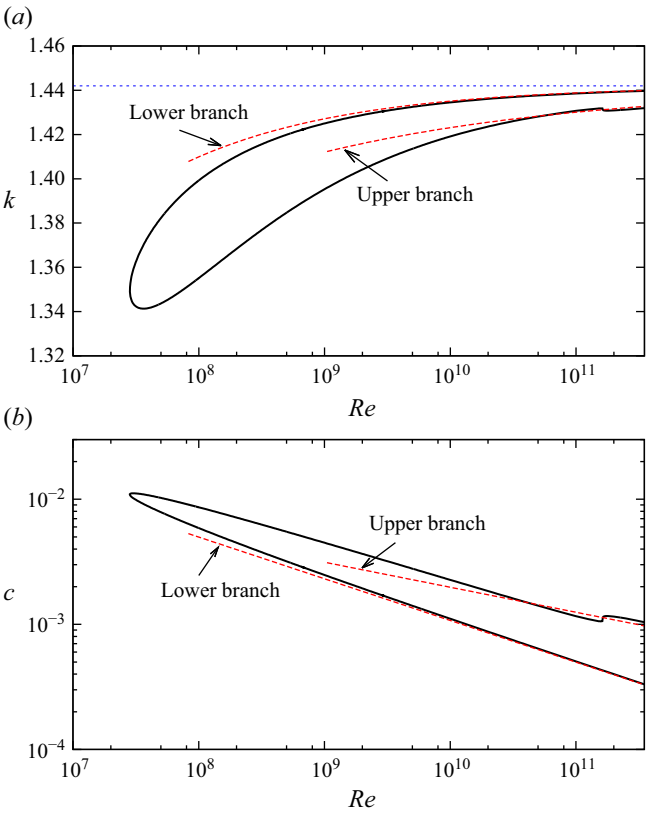

Figure 3. (*a*) Neutral curve of the narrow-gap Taylor–Couette flow problem (2.11) for $\alpha = 0.978$, $a = 0$ and (*b*) the corresponding phase speed c. The full numerical stability results are shown by the black solid curves. The dashed curves are the large-Re asymptotic results (2.28), (2.30) and (2.45). The blue dotted line in panel (*a*) is the leading-order approximation $k = 1.442$ obtained by (2.16). The numerical resolution is verified using up to 3000 Chebyshev modes.

In the inviscid core region, we expand the flow field as

$$u = u_0(y) + \epsilon u_1(y) + \cdots, \qquad v = v_0(y) + \epsilon v_1(y) + \cdots. \tag{2.12}$$

Substituting (2.12) into (2.11), retaining only the leading-order terms and eliminating v_0, we have the single second-order ordinary differential equation

$$\mathscr{L}u_0 = 0, \qquad \mathscr{L} \equiv \partial_y^2 + k_0^2\left(\frac{2}{\alpha^2 y} - 1\right). \tag{2.13}$$

A similar manipulation at the next order yields the inhomogeneous version of the equation

$$\mathscr{L}u_1 = -\left\{\frac{4k_0^2 c_1}{\alpha^2 y^2} + 2k_1 k_0\left(\frac{2}{\alpha^2 y} - 1\right)\right\} u_0. \tag{2.14}$$

From the no-penetration condition at the wall, we impose $u_0(1) = u_1(1) = u_0(0) = 0$. However, it will turn out from the boundary layer analysis that $u_1(0)$ cannot be zero, so we denote this displacement velocity as $U_d = u_1(0)$.

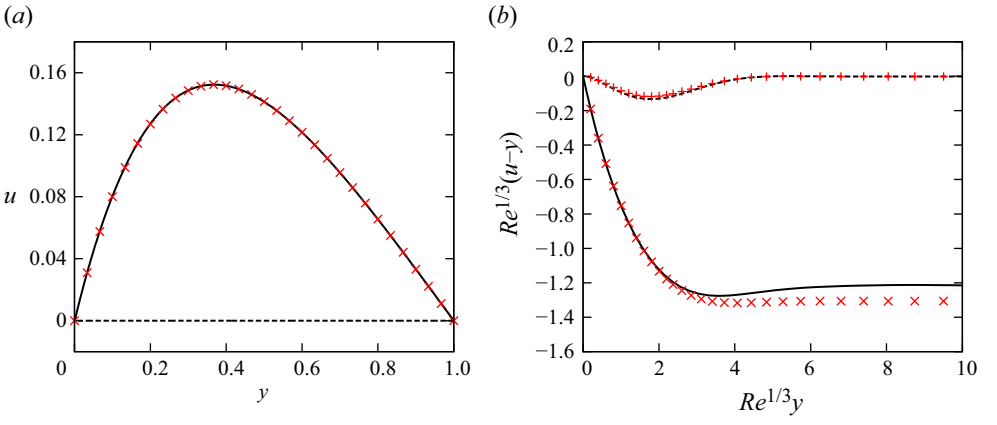

Figure 4. Comparison of the eigenfunctions between the linearised Navier–Stokes computations (lines) and asymptotic predictions (symbols). (*a*) Comparison of results without scaling the wall-normal coordinate. The solid and dashed curves are the real and imaginary parts of the lower branch neutral eigenfunction at $(Re, \alpha, k, a) = (10^{10}, 0.978, 1.434, 0)$. The points are the leading-order core solution u_0 with $(\alpha, k_0) = (0.978, 1.442)$; see (2.15). Note that u_0 attains its maximum value of 0.1523 at $y = 0.3698$, and u is normalised to have the same property. (*b*) Comparison in terms of the viscous wall layer scaling. The points are $U_0 - Y$, where U_0 is the leading-order wall-layer solution (2.22) with $(\alpha, k_0, k_1, c_1) = (0.978, 1.442, -14.9, 2.31)$ and Y is the stretched coordinate $Y = Re^{1/3}y$. Note that the eigenfunction is neutral, and thus the real part of the asymptotic solution approaches U_d as $Y \to \infty$.

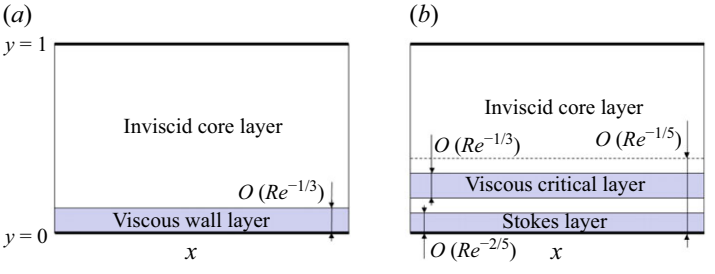

Figure 5. Sketch of large-Re asymptotic structure of (*a*) the lower branch type and (*b*) the upper branch type. A Stokes layer of thickness $O(Re^{-1/2})$ exists near $y = 1$, but it is omitted.

The no-slip conditions at the outer cylinder ($y = 1$) are satisfied through a Stokes layer of thickness $O(Re^{-1/2})$. However, this layer is passive and does not need to be analysed.

The leading-order core system is an eigenvalue problem for the eigenvalue k_0^2. The solution can be written down using Kummer's function of the first kind M:

$$u_0(y) = ye^{-k_0 y}\frac{M(\gamma, 2, 2k_0 y)}{M(\gamma, 2, 0)}, \qquad \gamma \equiv 1 - \frac{k_0}{\alpha^2}. \tag{2.15}$$

The boundary condition at $y = 1$ is fulfilled only when

$$M(\gamma, 2, 2k_0) = 0. \tag{2.16}$$

The crosses in figure 2 are obtained by looking for the smallest positive k_0 that satisfies (2.16) for each γ. For a small α, the approximation

$$k_0 \approx \frac{5\pi}{8\sqrt{2}}\alpha \tag{2.17}$$

is available, thanks to the property of the Kummer's function (Abramowitz & Stegun 1965). Both results are useful for estimating the wavenumber region where instability might occur. For $\alpha = 0.978$ used in figure 3(*a*), the prediction by (2.16) gives $k_0 \approx 1.442$, which is shown by the blue dotted line in the figure. Also, the leading-order core solution (2.15) agrees very well with the numerically obtained neutral eigenfunction, as depicted in figure 4(*a*). Note that to simplify the subsequent analysis, we have normalised the eigenfunction imposing $u_0'(0) = 1$.

Within the viscous wall layer, we use the stretched variable $Y = y/\epsilon$, and expand the wall-normal and streamwise velocity components as

$$u = \epsilon U_0(Y) + \cdots, \qquad v = V_0(Y) + \cdots, \tag{2.18}$$

respectively. Here, the normalisation $u_0'(0) = 1$ and the existence of the displacement velocity $u_1(0) = U_d$ imply that $U_0 \sim Y + U_d$ for large Y to match the boundary layer solution to the core solutions. While at $Y = 0$, of course, V_0, U_0 and U_0' must vanish to satisfy the no-slip conditions. Substituting (2.18) and the Taylor expansion $v_b = \lambda y + \cdots$ into (2.11), the leading-order equations are obtained as

$$(i\alpha(\lambda Y - c_1) - \partial_Y^2)V_0 + \lambda U_0 = 0, \tag{2.19}$$

$$(i\alpha(\lambda Y - c_1) - \partial_Y^2)U_0'' = 0. \tag{2.20}$$

From (2.9), λ is simply unity when $a = 0$; however, for our later purposes, we will carry out the calculations while keeping the general λ. The change of the variable $\xi = \sigma Y + \xi_0$ with the constants $\xi_0 = -\sigma c_1/\lambda$ and $\sigma = (i\lambda\alpha)^{1/3}$ transforms (2.20) to Airy's equation for $\partial_\xi^2 U_0$:

$$(\xi - \partial_\xi^2)\partial_\xi^2 U_0 = 0. \tag{2.21}$$

After some algebra, the solution satisfying the boundary conditions can be found as

$$U_0 = \sigma^{-1}\left[\xi + \frac{1}{\kappa(\xi_0)}\left(-\xi\kappa(\xi) - \mathrm{Ai}'(\xi) + \mathrm{Ai}'(\xi_0)\right)\right]. \tag{2.22}$$

For large Y, the magnitude of the functions $\kappa(\xi) = \int_\xi^\infty \mathrm{Ai}(\check{\xi})\mathrm{d}\check{\xi}$ and $\mathrm{Ai}'(\xi)$ rapidly diminish. Therefore, referring to the aforementioned matching condition, the displacement velocity is found as

$$U_d = \frac{\mathrm{Ai}'(\xi_0)}{\sigma\kappa(\xi_0)} - \frac{c_1}{\lambda}. \tag{2.23}$$

This is the only information we need for the dispersion relation in the wall layer analysis. Hence, we do not solve (2.19) to find V_0.

The dispersion relation readily follows from the solvability condition for the inhomogeneous equation (2.14). The adjoint solution is merely u_0 because the homogeneous equation (2.13) is self-adjoint. Multiplying (2.14) by u_0 and integrating from 0 to 1,

$$\int_0^1 u_0 \mathscr{L} u_1 dy = -\int_0^1 \left\{\frac{4k_0^2 c_1}{\alpha^2 y^2} + 2k_1 k_0\left(\frac{2}{\alpha^2 y} - 1\right)\right\} u_0^2 \mathrm{d}y. \tag{2.24}$$

The left-hand side becomes U_d after integration by parts and using (2.13). Therefore, k_1 and c_1 are now linked by

$$-\frac{1}{(\lambda\alpha)^{1/3}}\frac{i^{5/3}\mathrm{Ai}'(\xi_0)}{\kappa(\xi_0)}+c_1\left(I_1-\frac{1}{\lambda}\right)+k_1 I_2=0, \tag{2.25}$$

where

$$I_1(\alpha)=\frac{4k_0^2}{\alpha^2}\int_0^1\frac{u_0^2}{y^2}\mathrm{d}y, \qquad I_2(\alpha)=2k_0\int_0^1\left(\frac{2}{\alpha^2 y}-1\right)u_0^2\mathrm{d}y, \tag{2.26}$$

and $\xi_0=i^{7/3}(\lambda\alpha)^{1/3}c_1/\lambda$.

If the mode is neutral (i.e. c_1 is purely real), the imaginary part of (2.25) yields

$$\Im\left\{\frac{i^{5/3}\mathrm{Ai}'(i^{7/3}s)}{\kappa(i^{7/3}s)}\right\}=0, \qquad s=(\lambda\alpha)^{1/3}c_1/\lambda. \tag{2.27}$$

A real root of this function can be found at $s=s_0\approx 2.2972$ (Miles 1960). Setting $\lambda=1$, the following approximation is obtained for the lower branch shown in figure 3(*b*):

$$c=2.2972(0.978Re)^{-1/3}. \tag{2.28}$$

The real part of (2.25) can now be solved for k_1:

$$k_1=\frac{q_0+s_0(1-I_1)}{\alpha^{1/3}I_2}, \qquad q_0=\frac{i^{5/3}\mathrm{Ai}'(i^{7/3}s_0)}{\kappa(i^{7/3}s_0)}\approx -1.00. \tag{2.29}$$

The integrals (2.26) can be worked out numerically after substituting u_0 found in (2.15). For $\alpha=0.978$, using $k_0=1.442$ estimated before, the right-hand side of (2.29) can be computed as approximately 14.9. Therefore, we have the asymptotic result

$$k=1.442-14.9Re^{-1/3} \tag{2.30}$$

used in figure 3(*a*). The wall layer solution (2.22) is compared with the numerical neutral solution in figure 4(*b*).

2.4. *Upper branch asymptotic analysis*

The analysis for the upper branch is more complicated, and thus the neutrality of the perturbation is assumed from the beginning to facilitate discussion. The critical difference to the lower branch is that the majority of the wall layer becomes inviscid. Viscosity acts within two thinner sublayers: the critical layer sitting in the middle of the inviscid zone and the Stokes layer adjacent to the wall (see figure 5*b*).

The core structure is identical to the lower branch case, but the wall layer thickness, again denoted as ϵ, is different. Within the wall layer, the radial perturbation velocity is $O(\epsilon)$ to leading order, and it is merely a linear profile. Since the critical layer appears within the wall layer, the phase speed c must be $O(\epsilon)$. A displacement velocity induced across the critical layer affects the next-order component of the wall layer radial velocity, which is $O(\epsilon^2)$. A displacement velocity is also induced by the Stokes layer, and it must match to the contribution from the critical layer. The former velocity is proportional to the Stokes layer thickness Δ, so we require $\Delta=\epsilon^2$. Finally, by balancing the $O(c)$ advection term in (2.11) with the $O(Re^{-1}\Delta^{-2})$ diffusion term within the Stokes layer, we arrive at the scaling $\epsilon=Re^{-1/5}$ and $\Delta=Re^{-2/5}$. The critical layer thickness $\tilde{\epsilon}=Re^{-1/3}$ is indeed thinner than the wall layer thickness ϵ.

We begin the formal asymptotic analysis by writing $k=k_0+\epsilon k_1+\cdots$ and $c=\epsilon c_1+\cdots$. Within the wall layer, the perturbation velocity components are

expanded as

$$u = \epsilon U_0(Y) + \epsilon^2 U_1(Y) + \cdots, \qquad v = V_0(Y) + \epsilon V_1(Y) + \cdots, \tag{2.31}$$

where $Y = y/\epsilon$. Substituting them into (2.11), the leading-order equations are obtained as

$$i\alpha(Y - c_1)V_0 + U_0 = 0, \tag{2.32a}$$

$$i\alpha(Y - c_1)U_0'' = 0, \tag{2.32b}$$

and the next-order equations are

$$i\alpha(Y - c_1)V_1 + U_1 = 0, \tag{2.33a}$$

$$i\alpha(Y - c_1)U_1'' + 2Yk_0^2 V_0 = 0. \tag{2.33b}$$

For U_0, we impose $U_0(0) = 0$ to satisfy the non-penetrating condition on the wall. Also, $U_0 \sim Y + U_d$ as $Y \to \infty$ to match the normalised core solution. Then, the solution to the leading-order problem can be found as

$$U_0 = Y, \qquad V_0 = -\frac{Y}{i\alpha(Y - c_1)}, \tag{2.34}$$

which yields $U_d = 0$. The singularity that appears in V_0 should be resolved within the critical layer around $Y = c_1$. Given V_0, we can integrate (2.33*b*) twice to find

$$U_1 = -\frac{k_0^2}{\alpha^2}\Big\{(Y - c_1)^2 + 4c_1(Y - c_1)[\ln|Y - c_1| + \phi] - 2c_1^2[\ln|Y - c_1| + \psi]\Big\}. \tag{2.35}$$

The constants ϕ and ψ are unknown and may differ for $Y > c_1$ and $Y < c_1$. To distinguish the constants in the former region from those in the latter region, we attach a subscript $+$ to the former and $-$ to the latter. The constants ϕ_+ and ψ_+ must be purely real to match the core solution which is still inviscid at the corresponding order. The critical layer analysis reveals that

$$\phi_- = \phi_+ - i\pi, \qquad \psi_- = \psi_+ - i\pi. \tag{2.36}$$

This 'logarithmic phase-shift' may not be surprising to readers familiar with the asymptotic analysis of shear flows. To find this shift, one needs to use the expansions

$$u = \epsilon c_1 + \tilde{\epsilon}\zeta + O(\epsilon^2 \ln\epsilon) + \epsilon^2 \tilde{U}_1(\zeta) + O(\epsilon\tilde{\epsilon}\ln\epsilon) + \epsilon\tilde{\epsilon}\tilde{U}_2(\zeta) + \cdots, \tag{2.37a}$$

$$v = \epsilon\tilde{\epsilon}^{-1}\tilde{V}_0(\zeta) + \tilde{V}_1(\zeta) + \cdots, \tag{2.37b}$$

valid when $\zeta = \tilde{\epsilon}^{-1}(y - \epsilon c_1)$ is $O(1)$. Equations (2.35) and (2.36) imply that

$$\Im(u) \to -\epsilon^2 \frac{6\pi c_1^2 k_0^2}{\alpha^2} \qquad \text{as} \qquad Y \to 0. \tag{2.38}$$

Within the Stokes layer, we write $Z = y/\epsilon^2$ and expand

$$u = \epsilon^2 \check{U}_0(Z) + \cdots, \qquad v = \check{V}_0(Z) + \cdots. \tag{2.39}$$

The no-slip boundary conditions are written as $\check{V}_0(0) = \check{U}_0(0) = \check{U}_0'(0) = 0$. Substitution of (2.39) to (2.11) yields the leading-order equations

$$(i\alpha c_1 + \partial_Z^2)\check{V}_0 = 0, \qquad (i\alpha c_1 + \partial_Z^2)\check{U}_0'' = 0. \tag{2.40}$$

The solution of the second equation, which does not grow exponentially for large Z, can be found as follows:

$$\breve{U}_0 = Z + \frac{e^{-qZ} - 1}{q}, \qquad q = (1 - i)\sqrt{\frac{\alpha c_1}{2}}. \tag{2.41}$$

The exponential part is negligible when Z is large. Thus, at the outer edge of the Stokes layer,

$$\Im(u) \to -\epsilon^2 \frac{1}{(2\alpha c_1)^{1/2}} \qquad \text{as} \qquad Z \to \infty. \tag{2.42}$$

Matching (2.38) and (2.42), the scaled phase speed is found as

$$c_1 = \frac{\alpha^{3/5}}{2^{1/5}(6\pi k_0^2)^{2/5}}. \tag{2.43}$$

Here, we can use (2.16) to find k_0, as the core analysis is identical to that for the lower branch case, while the dispersion relation (2.29) simplifies to

$$k_1 = -\frac{c_1 I_1}{I_2} \tag{2.44}$$

because $u_1(0) = U_d = 0$, as remarked just below (2.34).

Substitution of $\alpha = 0.978$ and $k_0 = 1.442$ into (2.43) and (2.44) gives $c_1 \approx 0.198$ and $k_1 \approx 1.89$. The asymptotic approximations shown in figure 3 are thus obtained as

$$c = 0.198 Re^{-1/5}, \qquad k = 1.442 - 1.89 Re^{-1/5}. \tag{2.45}$$

3. Wide-gap Taylor–Couette flow

The analysis presented so far can be extended to the full Taylor–Couette flow problem introduced in § 2.1. The radius ratio η now takes the value between 0 and 1, and the rotation ratio a defined in (2.5) is not necessarily zero.

Substituting

$$\begin{aligned}(u, v, w, p) = &\left(0, R_o\, r\Omega(r), 0, R_o^2 \int^r r_* \Omega^2(r_*) \mathrm{d}r_*\right) \\ &+ (\hat{u}(r), \hat{v}(r), \hat{w}(r), R_o\, \hat{p}(r)) \exp(im(\theta - R_o\, ct) + ikz) + \text{c.c.}\end{aligned} \tag{3.1}$$

into (2.1), linearising the equations and removing the hats, we have the well-known eigenvalue problem:

$$\mathcal{L}u - 2\Omega v + \frac{1}{R_o}\left(\frac{u}{r^2} + \frac{2imv}{r^2}\right) = -p', \tag{3.2a}$$

$$\mathcal{L}v + (2\Omega + r\Omega')u + \frac{1}{R_o}\left(\frac{v}{r^2} - \frac{2imu}{r^2}\right) = -\frac{im}{r}p, \tag{3.2b}$$

$$\mathcal{L}w = -ikp, \tag{3.2c}$$

$$u' + \frac{u}{r} + \frac{im}{r}v + ikw = 0. \tag{3.2d}$$

The no-slip conditions $u = v = w = 0$ are imposed at $r = r_i$ and r_o. To compactly write the equations, we introduced the linear operator $\mathcal{L} = im(\Omega - c) - R_o^{-1}(\partial_r^2 + r^{-1}\partial_r - r^{-2}m^2 - k^2)$. The physically realisable velocity field must have a 2π periodicity in the θ-direction; therefore, m must be an integer.

Section 3.1 extends the lower branch type asymptotic analysis deduced in § 2.3 for the narrow-gap limit case. In view of (3.2), it is clear that the suitable large asymptotic parameter is R_o. Recall that Ω depends on the parameter a. We only study small enough $|a|$, so that the non-zero rotation ratio effect preserves the asymptotic structure studied in § 2.3. The angular velocity (2.4) of the circular Couette flow hence admits the Taylor expansion $\Omega = \Omega_0 + a\Omega_1 + \cdots$, where

$$\Omega_0 = \frac{1}{1+\eta} - \frac{r_i^2}{r^2(1+\eta)}, \quad \Omega_1 = -\frac{\eta^2}{1+\eta} + \frac{r_i^2}{r^2(1+\eta)}. \tag{3.3}$$

In § 3.2, the asymptotic results are compared with the full numerical solution of (3.2).

The extension of the upper branch theory in § 2.4 to the wide-gap case is straightforward, but given its limited practical importance, we omit this discussion.

3.1. *Lower branch asymptotic analysis*

We introduce a small parameter $\epsilon = R_o^{-1/3}$ that describes the thickness of the wall layer near the inner cylinder. Note that this ϵ is not the same as that used in § 2.3; we will clarify their relationship later. The rotation rate a is taken to be $O(\epsilon)$ so that $a_1 = a/\epsilon$ is of order unity. The azimuthal wavenumber m is held fixed, while the axial wavenumber and the complex phase speed are written in the forms $k = k_0 + \epsilon k_1 + \cdots$ and $c = \epsilon c_1 + \cdots$, respectively.

In the inviscid core region, we expand

$$(u, v, w, p) = (u_0, v_0, w_0, p_0) + \epsilon(u_1, v_1, w_1, p_1) + \cdots . \tag{3.4}$$

The terms appearing on the right-hand side are all functions of r. Substitution of those expansions to (3.2) yields the leading-order equation for $u_0(r)$,

$$\mathscr{L}u_0 = 0, \tag{3.5}$$

and the next-order equation for $u_1(r)$,

$$\mathscr{L}u_1 = k_1 F_2 u_0' - (c_1 F_0 + k_1 F_1 + a_1 F_3)u_0. \tag{3.6}$$

The differential operator $\mathscr{L}$ and the functions F_0, F_1, F_2 and F_3 depend on m, k_0, η, as can be found in the Appendix. The boundary conditions are $u_0(r_i) = u_0(r_o) = u_1(r_o) = 0$ and $u_1(r_i) = U_d$, where U_d is the displacement velocity to be found by the wall layer analysis.

Within the wall layer near the inner cylinder, the suitable expansions are

$$(u, v, w, p) = (\epsilon U_0, V_0, W_0, \epsilon P_0) + \cdots , \tag{3.7}$$

where the terms on the right-hand side are functions of $Y = \epsilon^{-1}(r - r_i)$. Within the layer where Y is of order unity, the base-flow angular velocity (2.4) behaves like $\Omega = \epsilon(\lambda Y + ba_1) + \cdots$ with the constants

$$\lambda \equiv \Omega_0'(0) = \frac{2}{r_i(1+\eta)}, \qquad b \equiv \Omega_1(0) = 1 - \eta. \tag{3.8}$$

After some manipulations, from the leading-order problem, we can find that $U_0(Y)$ satisfies

$$(im(\lambda Y + ba_1 - c_1) - \partial_Y^2)U_0'' = 0 \tag{3.9}$$

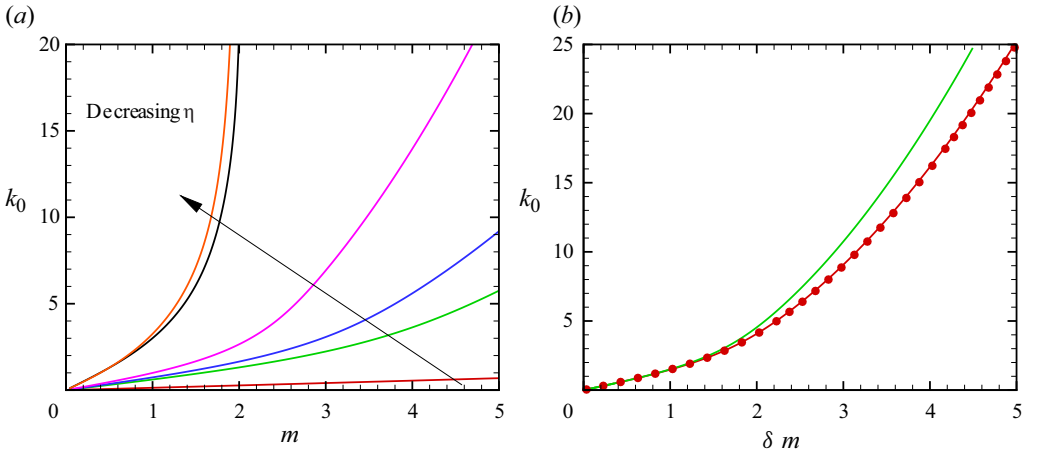

Figure 6. Asymptotic results obtained by numerically solving (3.5). (*a*) Dependence of the leading-order axial wavenumber k_0 on the azimuthal wavenumber m for $\eta = 0.99$ (red), 0.8 (green), 5/7 (blue), 0.5 (pink), 0.1 (black), 0.01 (orange). (*b*) The red and green curves are the results for $\eta = 0.99$ and 0.8, respectively, shown in the $\delta\, m$–k_0 plane. The circles are the narrow-gap limit results assuming $(k_0, \delta\, m) = (\bar{k}_0, \alpha)$.

which, after re-reading m, $(c_1 - ba_1)$ as α, c_1, coincides with (2.20). Therefore, we can reuse the narrow-gap result to obtain the displacement velocity

$$U_d = -\frac{i^{5/3}\mathrm{Ai}'(\xi_0)}{(\lambda m)^{1/3}\kappa(\xi_0)} - \frac{c_1 - ba_1}{\lambda}, \qquad \xi_0 = \frac{i^{7/3}(\lambda m)^{1/3}(c_1 - ba_1)}{\lambda}. \tag{3.10}$$

To solve the inhomogeneous problem (3.6), we use the inner product $\langle f, g\rangle \equiv \int_{r_i}^{r_o} fg\mathrm{d}r$. The homogeneous problem (3.5) is not self-adjoint, so we introduce the adjoint problem

$$\mathscr{L}^{\dagger} u^{\dagger} = 0, \qquad u^{\dagger}(r_i) = u^{\dagger}(r_o) = 0, \tag{3.11}$$

where the operator $\mathscr{L}^{\dagger}$ is given in the Appendix. The solution $u^{\dagger}(r)$ of this problem with the normalisation $(\hat{u}^{\dagger})'(r_i) = 1$ can be uniquely determined. Taking the inner product of $u^{\dagger}$ and (3.6), we obtain the dispersion relation

$$U_d + \langle u^{\dagger}, F_0 u_0\rangle c_1 - k_1\langle u^{\dagger}, F_2 u_0' - F_1 u_0\rangle + a_1\langle u^{\dagger}, F_3 u_0\rangle = 0, \tag{3.12}$$

where $U_d(m, \eta, c_1, a_1)$ is given in (3.10).

3.2. *Numerical analysis*

The wide-gap version of the asymptotic results requires numerical work to extract useful information. First, the leading-order problem, (3.5) and the associated boundary conditions, needs to be solved. The two boundary conditions can be satisfied only when specific values of $k_0(m, \eta)$ are taken. The admissible values of k_0 for various η are summarised in figure 6(*a*). Only integer values of m are physically relevant, though real values of m can be used in numerical computation without issue. If the perturbations are assumed to be neutral, the next step is to find $c_1(m, \eta, a_1)$ from the imaginary part of (3.12). Then the real part of (3.12) can be used to compute $k_1(m, \eta, a_1)$ after some numerical integrations. The dependence of k_1 on a_1 is perfectly linear, as shown in figure 7(*a*) for the case $m = 1$.

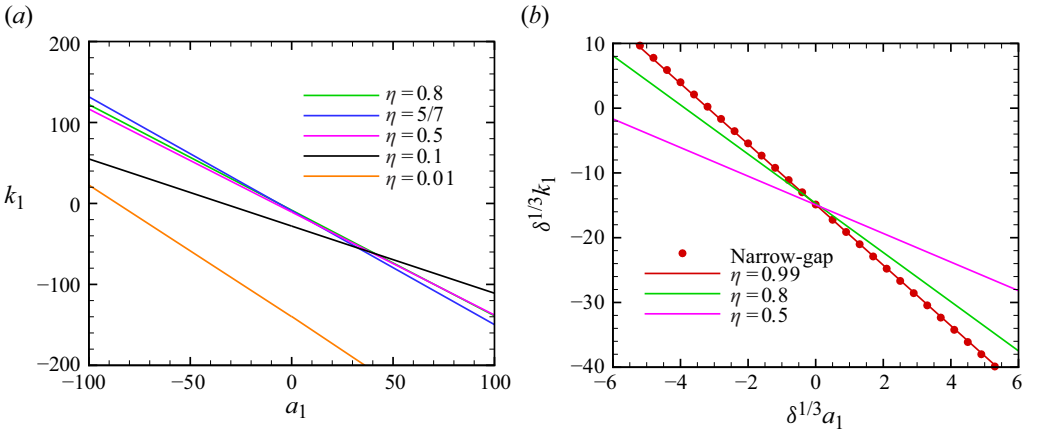

Figure 7. Dependence of k_1 on a_1 for the neutral modes computed by (3.12). (*a*) Results for wide-gap configurations. The azimuthal wavenumber is fixed at $m = 1$. (*b*) Results for narrow-gap configurations. The azimuthal wavenumber is varied as $m = 0.978/\delta$ to observe the convergence to the narrow-gap results with $\alpha = 0.978$ (circles). In the narrow-gap results, we set $(\delta^{1/3}k_1, \delta^{1/3}a_1) = (\overline{k}_1, \overline{a}_1)$.

Now, let us explore the connection between the numerical analysis presented in this section and the narrow-gap limit analysis discussed in § 2.3. Recall that in the latter analysis, we required $Re = \delta\, R_o = \sqrt{1-\eta}\, R_o$ to be large to define the small parameter $\overline{\epsilon} = Re^{-1/3}$. Here, the overline is added to distinguish from $\epsilon = R_o^{-1/3}$ defined in § 3.1; likewise, we use $\overline{k}_0$, $\overline{k}_1$, $\overline{c}$ and $\overline{c}_1$ to denote the corresponding quantities that appeared in § 2.3. The two wavenumber expansions $k = \overline{k}_0 + \overline{\epsilon}\overline{k}_1 + \ldots$ and $k = k_0 + \epsilon k_1 + \ldots$ imply the equivalence $\overline{k}_0 = k_0$ and $\overline{k}_1 = \delta^{1/3}k_1$. Of course, to observe the convergence to the narrow-gap result, we must set $\alpha = \delta\, m$ because the wavenumber α is defined on the variable x. Also, from the growth rate equality $i\alpha Re\overline{c} = im R_o c$, we expect $\overline{c}_1 = \delta^{-5/3}c_1$ to hold. Moreover, we write $\overline{a}_1 = \delta^{1/3}a_1$ because, with this and the above rescaling, in the limit $\eta \to 1$, the dispersion relation (3.12) reduces to

$$-\frac{1}{\alpha^{1/3}}\frac{i^{5/3}\mathrm{Ai}'(\overline{\xi}_0)}{\kappa(\overline{\xi}_0)} + \overline{c}_1(I_1 - 1) + \overline{k}_1 I_2 + \overline{a}_1\left(1 - \frac{I_1}{2}\right) = 0, \tag{3.13}$$

where $\overline{\xi}_0 = i^{7/3}\alpha^{1/3}(\overline{c}_1 - \overline{a}_1)$. This is precisely a generalisation of (2.25) for non-zero rotation rates. The convergence of k_0 to the narrow-gap result as $\eta \to 1$ is graphically evident in figure 6(*b*). Figure 7(*b*) depicts the similar excellent convergence to the narrow-gap result for the a_1–k_1 relation. The narrow-gap result in this figure was produced by (3.13) for $m = 0.978/\delta$, so the value of $\overline{k}_1$ at $a_1 = 0$ corresponds to the lower branch asymptotic curve seen in figure 3(*a*).

The dispersion relation (3.12) can also be used for non-neutral modes. Figure 8 presents the scaled growth rate computed by the asymptotic analysis. Panels (*a*) and (*b*) are the results for $\eta = 5/7$, $m = 2$, which are used by Deguchi (2017). The value of k_0 is found as 1.651 from (3.5), and the variation of $c_{1i} = \Im(c_1)$ on k_1 for $a_1 = 0$ can be found by (3.12) as the circles in panel (*a*). The solid curves represent the full Navier–Stokes computations based on (3.2), which, as expected, converge to the asymptotic results as Re increases. To compare the results, we plotted $R_o^{1/3}c_i$ against $R_o^{1/3}(k - k_0)$; recall the scaling described just above (2.12). The flow becomes unstable when $k_1 \approx R_o^{1/3}(k - k_0)$ is smaller than -20, with the growth rate reaching its maximum around $k_1 = -46.0$. Fixing k_1 at this value and

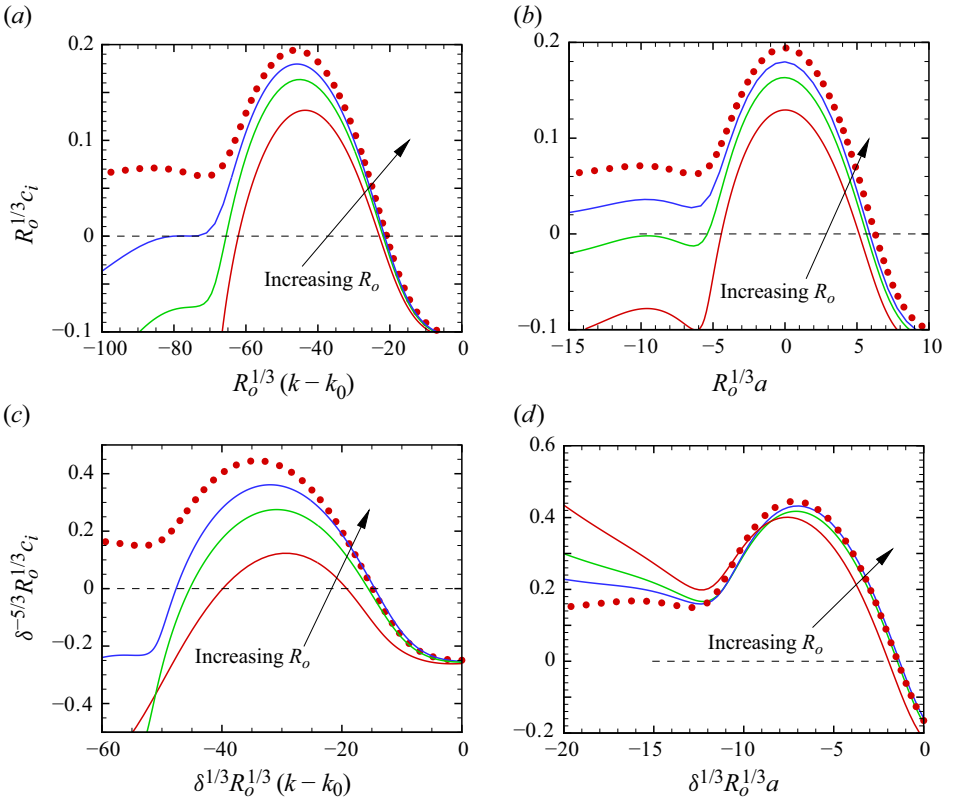

Figure 8. The scaled growth rate. In panels (*a*) and (*b*), the wide gap $\eta = 5/7$ is used with $m = 2$. The red, green and blue curves are the linearised Navier–Stokes results for $R_o = 10^9$, 10^{10} and 10^{11}, respectively. The symbols are the asymptotic results. (*a*) $a = 0$; (*b*) $k = k_0 + R_o^{-1/3}k_1$ with $(k_0, k_1) = (1.651, -46.0)$. The circles are computed by the wide-gap formula (3.12). Panels (*c*) and (*d*) are similar results but for the narrow gap $\eta = 0.99$ with $m = 0.978/\delta$. (*c*) $a = 0$ with $(k_0, a_1) = (1.442, 0)$; (*d*) $k = k_0 + R_o^{-1/3}k_1$ with $(k_0, k_1) = (1.15, -10)$. The asymptotic computation uses the narrow-gap limit formula (3.13) with $\alpha = 0.978$.

varying a_1 results in panel (*b*). An increase in the rotation rate has a stabilising effect. To observe the convergence in the Navier–Stokes results, we set $k = k_0 + R_o^{-1/3}k_1$.

Figures 8(*c*) and 8(*d*) compare the linearised Navier–Stokes results for $\eta = 0.99$ (curves) with the narrow-gap asymptotic results (circles). Again, we choose $\alpha = 0.978$ used in § 2 for the asymptotic computation. Thus, k_0 is found as 1.442 by (2.16), and in panel (*c*), where c_{1i} is plotted against k_1 for $a_1 = 0$, the neutral point $k_1 \approx -14.9$ recovers the approximation (2.30). In the Navier–Stokes computations, the choice $\eta = 0.99$ implies that the suitable azimuthal wavenumber is $m = 0.978/\delta = 9.78$. The asymptotic convergence of the numerical data $(\delta^{-5/3}R_o^{1/3}c_i,\ \delta^{1/3}R_o^{1/3}(k-k_0))$ towards $(\bar{c}_{1i}, \bar{k}_1)$ computed by (3.13) is reasonable, considering that there are now two factors causing errors: the finiteness of δ and Re^{-1}. Even if we choose the closest integer value of $m = 10$, the result does not differ significantly. Panel (*d*) shows the similar comparison, but now the rotation rate is varied for fixed $k_1 = -10$. Overall, we can observe the similar trend as the wide-gap case. Figure 9 illustrates a comparison between the eigenfunction of the linearised Navier–Stokes equations (3.2) and the solution of the asymptotic problem. All the above results

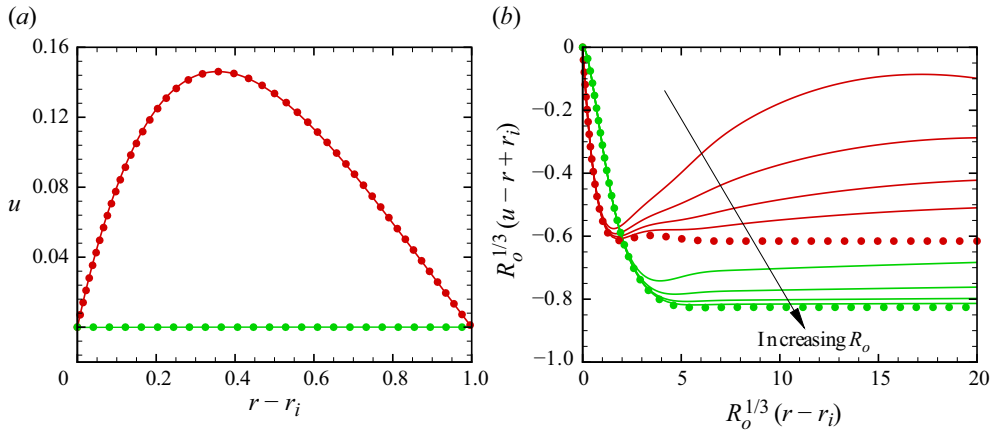

Figure 9. Comparison of the eigenfunctions between the leading-order asymptotic predictions (symbols) and the linearised Navier–Stokes results (lines) with $R_o = 10^{10}$, 10^{11}, 10^{12} and 10^{13}. The parameters are $\eta = 5/7$, $a = 0$, $m = 2$ and $k = 1.65$, where the mode is unstable. Red, real part; green, imaginary part. (*a*) Comparison in terms of the inviscid core scaling. (*b*) Comparison in terms of the viscous wall layer scaling.

unequivocally demonstrate the convergence of the Navier–Stokes computation towards the asymptotic results.

Instability occurs for all values of $\eta \in (0, 1)$, if R_o is large enough. This is demonstrated in figure 6, where the case of a stationary inner cylinder case ($a = 0$) is shown. Of particular interest from an application point of view is the extent to which the D17 mode can penetrate into the Rayleigh stable region, i.e. how much we can increase the rotation rate a before the flow completely stabilises. Figure 7 shows that the lower branch type instability always exists as long as a is $O(R_o^{-1/3})$. The upper branch type survives a bit larger a of $O(R_o^{-1/5})$. When a reaches $O(1)$, the stability is determined by the inviscid problem similar to (3.5), but with a critical layer located away from the walls (Drazin & Reid 1981; Billant & Gallaire 2005; Caillol & Maslowe 2007). This type of instability may appear when the wavenumbers are fixed and the Reynolds number is increased. For the narrow-gap limit case, taking long wavelengths $k = O(Re^{-1})$ and $\alpha = O(Re^{-1})$ leads to another large-Re asymptotic limit of instability for $a = O(1)$, However, this limit, similar to that considered by Cowley & Smith (1985), cannot be realised for wide gaps, since m must be an asymptotically small non-zero number. Continuing the neutral curve for general a using (3.2) is a computationally challenging task, so we do not pursue further investigation.

4. A boundary layer flow over a convex wall

Here we consider a near-wall boundary layer flow influenced by weak wall curvature. Rational analysis of this problem in the high-Reynolds-number asymptotic limit was established by Hall (1982, 1983, 1988) for concave wall cases. Our theory developed in the previous sections applies when the wall is convex and the magnitude of the Görtler number G, as defined by Hall, is sufficiently large. To demonstrate this, here we employ the simplest set-up: the asymptotic suction boundary layer (Hocking 1975; Milinazzo & Saffman 1985; Fransson & Alfredsson 2003).

In this flow configuration, the boundary layer thickness remains unchanged downstream due to suction from the wall. Therefore, the complexity associated with non-parallel effects, such as those present in the Blasius boundary layer, can be avoided.

4.1. *Asymptotic suction boundary layer*

The generalised version of the instability theory for the asymptotic suction boundary layer, incorporating the effect of wall curvature, can be naturally derived from Taylor–Couette flow by writing the boundary conditions as follows:

$$\mathbf{v}(r_i, \theta, z) = (-S, R_i, 0), \quad \mathbf{v}(r_o, \theta, z) = (-\eta S, R_o, 0). \tag{4.1}$$

Here, S represents the non-dimensional suction velocity on the inner cylinder, which introduces a uniform radial cross-flow; the same flow configuration was studied by Gallet *et al.* (2010). The base flow solution can be found to be $(u, v, w) = (-(r_i/r)S, R_o r\Omega, 0)$, with the function $\Omega(r)$ in the azimuthal component modified as

$$\Omega = Ar^{-r_i S} + B/r^2, \qquad A = \frac{1}{r_o^{1-r_i S}} \frac{1-\eta^2 a}{1-\eta^{2-r_i S}}, \qquad B = r_i \frac{\eta a - \eta^{1-r_i S}}{1-\eta^{2-r_i S}}. \tag{4.2}$$

The associated stability problem is governed by (3.2), but the linear operator must include the cross-flow effect as $\mathcal{L} = im(\Omega - c) - R_o^{-1}(\partial_r^2 + (r_i S/r)\partial_r + r^{-1}\partial_r - r^{-2}m^2 - k^2)$.

If we take large values of S, the base flow develops a boundary layer near the inner cylinder. For simplicity, we set $a = 0$. Then, it is easy to check that as $S \to \infty$, the base flow behaves as

$$v \sim \frac{R_o r_o}{r} + O(S^{-1}) \qquad \text{if } r - r_i = O(1), \tag{4.3}$$

$$v \sim \frac{R_o}{\eta}(1 - e^{-y}) + O(S^{-1}) \qquad \text{if } y = S(r - r_i) = O(1). \tag{4.4}$$

This observation suggests that the boundary layer thickness is $O(S^{-1})$.

To clarify the connection with the standard boundary layer analysis, we apply the following manipulations.

(i) Replace the length scale with one based on boundary layer thickness, using y and the wavenumbers $\beta \equiv S^{-1}k$ and $\alpha \equiv m/Sr_i$.
(ii) Denote (v, u, w) as (u_x, u_y, u_z) to express the equations in the familiar form used the boundary layer analysis. Also, rewrite ηp as p.
(iii) Redefine the Reynolds number as $Re \equiv R_o/\eta S$, and write $u_{xb} \equiv r_i \eta \Omega$ and $C = r_i \eta c$. This Reynolds number is naturally defined by the free stream velocity at the edge of the boundary layer and the boundary layer thickness.

These transformations recast the stability problem into

$$\mathcal{L}u_x + \left(2\frac{u_{xb}}{Sr_i} + \frac{r}{r_i}\frac{du_{xb}}{dy}\right)u_y - \frac{r_i}{r^2 SRe}u_y + \frac{1}{SRe}\left(\frac{u_x}{Sr^2} - \frac{2ir_i\alpha u_y}{r^2}\right) = -i\alpha\frac{r_i}{r}p, \tag{4.5a}$$

$$\mathcal{L}u_y - 2\frac{u_{xb}}{Sr_i}u_x + \frac{r_i}{r^2 SRe}u_y + \frac{1}{SRe}\left(\frac{u_y}{Sr^2} + \frac{2ir_i\alpha u_x}{r^2}\right) = -\frac{dp}{dy}, \tag{4.5b}$$

$$\mathcal{L}u_z = -i\beta p, \tag{4.5c}$$

$$i\alpha\frac{r_i}{r}u_x + \frac{du_y}{dy} + \frac{u_y}{Sr} + i\beta u_z = 0, \tag{4.5d}$$

where $\mathcal{L} = i\alpha(u_{xb} - C) - Re^{-1}(\partial_y^2 + (r_i/r)\partial_y + S^{-1}r^{-1}\partial_y - (r_i/r)^2\alpha^2 - \beta^2)$. No asymptotic approximations have been made at this stage, provided that Ω defined in (4.2) is used. Therefore, together with the no-slip conditions on the cylinder walls, the linearised problem remains valid throughout the entire annular region.

If S is large, the stability problem may be simplified to

$$\mathcal{L}u_x + u'_{xb}u_y = -i\alpha p, \qquad \mathcal{L}u_y = -p' + g u_{xb}u_x, \tag{4.6a}$$

$$\mathcal{L}u_z = -i\beta p, \qquad i\alpha u_x + u_y{}' + i\beta\, u_z = 0, \tag{4.6b}$$

where $\mathcal{L} = \mathrm{i}\alpha(u_{xb} - c) - Re^{-1}(\partial_y^2 + \partial_y - \alpha^2 - \beta^2)$, $u_{xb} = 1 - e^{-y}$ and $g = 2/Sr_i$. The primes denote derivatives with respect to y. At $y = 0$, the no-slip conditions $u_x = u_y = u_z = 0$ are imposed, and we assume the perturbations vanish as $y \to \infty$. The above boundary layer problem, formulated near the inner cylinder wall, constitutes an 'intermediate reduced system', as the magnitudes of the terms in (4.6) are not strictly balanced. To find the correct reduced system, a detailed asymptotic analysis in § 4.2 is required. Nonetheless, the same reduced problems are obtained whether the asymptotic analysis begins with (4.6) or (4.5), indicating that the former equations, despite their simplicity, include all the essential terms for the asymptotic reduction.

It should also be noted that the intermediate reduced system, excluding the Görtler term proportional to g, has the similar structure as the local stability problem of general boundary layer flows. The constant g is the parameter that represents the ratio of the boundary layer thickness to the radius of curvature of the wall. If the wavelengths are assumed to be comparable to the boundary layer thickness, the Görtler term is often omitted in the local stability studies. However, when the streamwise wavelength becomes sufficiently long, this term begins to significantly influence stability, as we shall see shortly.

In the context of the current parallel boundary layer problem, when the Görtler term is absent, (4.6) reduces to the Orr–Sommerfeld and Squire equations for the asymptotic suction boundary layer, where the onset of the instability is well known to occur at $(\alpha, \beta, Re) = (0.15547, 0, 27189)$; see Hocking (1975); Drazin & Reid (1981). The mechanism of this instability is essentially of the TS wave type. Note also that Görtler vortex type instabilities appear when $G = gRe^2$ is an $O(1)$ negative number, akin to Hall's (1983) work on growing boundary layers. In this case, we need to recover several terms we omitted from (4.5). As noted earlier, those terms do not affect our analysis that follows.

Figure 10 shows the neutral spanwise wavenumber β and phase speed c as the Reynolds number is varied, with the streamwise wavenumber fixed at $\alpha = 0.0036$. The red solid curves are computed by the intermediate boundary layer approximation (4.6) with $g = 2 \times 10^{-4}$; the flow becomes unstable in the region between them. The neutral curves closely match the green circles, which are the neutral points computed using the full linearised Navier–Stokes equations (4.5*d*) with $S = 50.25$. In the linearised Navier–Stokes computation, the radius ratio of the cylinders are chosen as $\eta = 0.995$, resulting in $g = 2(1 - \eta)/S\eta \approx 2 \times 10^{-4}$. The value of the azimuthal wavenumber is $m = 36$, which corresponds to $\alpha \approx 0.0036$. The Reynolds number, as mentioned earlier, has been rescaled as $Re = R_o/\eta S$.

In the figure, the black dashed curve represents the result for the pure asymptotic suction boundary layer case ($g = 0$). Comparing the black and red curves reveals that even small variations in g can cause significant changes in the shape of the neutral curve. At the large-Reynolds-number regime, the effect of wall curvature generates a new 'D17' instability in a narrow band of β. The asymptotic behaviour of the D17 modes can be explained by the lower and upper branch theories, analogues to those discussed in § 2, with the lower branch elaborated in § 4.2.

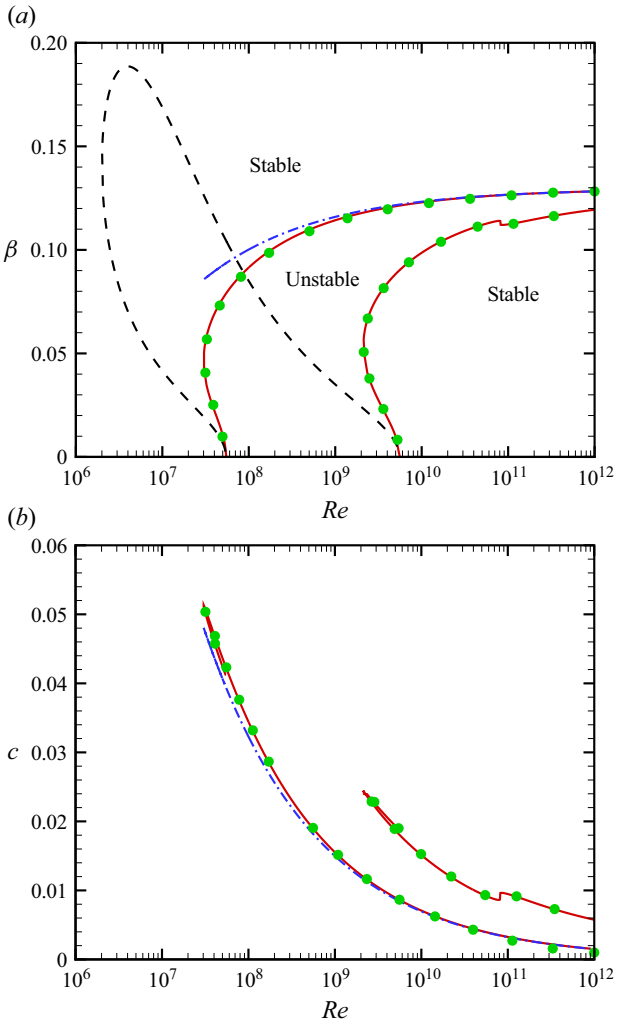

Figure 10. Linear stability of the asymptotic suction boundary layer. The streamwise wavenumber is fixed at $\alpha = 0.0036$. (*a*) The red solid curves represent the neutral curves for the convex wall case $g = 2 \times 10^{-4}$, with stable/unstable regions indicated by the labels. These results are computed using the intermediate reduced equations (4.6) within the boundary layer. The green circles show the same results, but they are computed using the full linearised Navier–Stokes equations (4.5*d*) with $S = 50.25$. The black dashed curve corresponds to the flat wall case $g = 0$. The blue dash-dotted curve is the asymptotic result given by (4.19) for $g = 2 \times 10^{-4}$. (*b*) Phase speed of the neutral modes for $g = 2 \times 10^{-4}$.

For spanwise-independent perturbations, we can theoretically show that the stability remains unchanged from the $g = 0$ case. Therefore, the unstable region at $g = 2 \times 10^{-4}$ represents a mixture of the TS mode and the D17 mode. Varying β from zero along the red curve illustrates a smooth transition from TS waves to D17 modes, with the Reynolds number reaching the minimum value $Re = 3.01 \times 10^7$ at $\beta = 0.0467$. Note that this Reynolds number is not a critical value, as it is not optimised across all wavenumber pairs. Clearly, for any value of g, the critical Reynolds number cannot fall below 27 819, which occurs at $\beta = 0$. We have confirmed that the critical Reynolds number remains at this value for $g = 2 \times 10^{-4}$. In general, for relatively large α, small values of g have no

significant impact on stability. Numerical computations were necessary to verify this, as Squire's theorem does not hold for $g \neq 0$.

4.2. *Lower-branch asymptotic analysis*

Here, we conduct a lower-branch-type matched asymptotic expansion analysis for the stability problem (4.5). The key assumptions in the asymptotic analysis, in addition to the largeness of S, are $Re \gg 1$ and $g \gg Re^{-2}$. The second condition is satisfied at the high-Reynolds-number limit if $g > 0$ is held constant.

The analysis proceeds along the same lines as in § 2.3. An inviscid main layer emerges at which $y = O(1)$, while the no-slip conditions are satisfied via the viscous wall layer of thickness $O(\epsilon)$ with $\epsilon = (gRe^2)^{-1/6} \ll 1$. Those regions are somewhat similar to the main deck and lower deck of the triple-deck theory, respectively, but a structure like the upper deck does not emerge. Using the small parameter ϵ, we expand the spanwise wavenumber and the phase speed as $\beta = \beta_0 + \epsilon\beta_1 + \cdots$ and $C = \epsilon C_1 + \cdots$, respectively. Also, we rescale the streamwise wavenumber as $\alpha = g^{1/2}\alpha_0$.

In the main layer, we write

$$\begin{bmatrix} u_x \\ u_y \\ u_z \\ p \end{bmatrix} = \begin{bmatrix} u_{x0}(y) + \epsilon u_{x1}(y) + \cdots \\ g^{1/2}(u_{y0}(y) + \epsilon u_{y1}(y) + \cdots) \\ g^{1/2}(u_{z0}(y) + \epsilon u_{z1}(y) + \cdots) \\ g(p_0(y) + \epsilon p_1(y) + \cdots) \end{bmatrix}. \tag{4.7}$$

Substituting (4.7) into (4.5) (or (4.6)), the leading-order equations can be combined to yield

$$\mathscr{L}u_{y0} = 0, \qquad \mathscr{L} = \partial_y^2 - \beta_0^2 - \frac{u''_{xb}}{u_{xb}} + \frac{\beta_0^2}{\alpha_0^2}\frac{u'_{xb}}{u_{xb}}. \tag{4.8}$$

While, as expected, the next-order equations yield the inhomogeneous equation

$$\mathscr{L}u_{y1} = \frac{C_1}{u_{xb}}\left(u''_{y0} - \beta_0^2 u_{y0} - \frac{\beta_0^2}{\alpha_0^2}\frac{u'_{xb}}{u_{xb}}u_{y0}\right) + 2\beta_0\beta_1\left(1 - \frac{1}{\alpha_0^2}\frac{u'_{xb}}{u_{xb}}\right)u_{y0}. \tag{4.9}$$

The non-trivial solution of (4.8) satisfying $u_{y0} = 0$ at $y = 0$ and $u_{y0} \to 0$ as $y \to \infty$ can be found as

$$u_{y0} = \lambda^{-1} u_{xb} e^{-\beta_0 y} \tag{4.10}$$

only when

$$\beta_0 = 2\alpha_0^2. \tag{4.11}$$

The constant λ represents the value of u'_{xb} at $y = 0$, and the factor λ^{-1} in (4.10) normalises $u'_{y0} = 1$ at $y = 0$. Note that when the sign of g is negative (i.e. in the case of a concave wall), constructing a non-trivial solution becomes impossible.

The solvability condition of the inhomogeneous equation (4.9) then determines the dispersion relation. The far-field condition $u_{y1} \to 0$ as $y \to \infty$ remains unchanged from the leading-order problem. Near the wall, however, the effect of the displacement velocity from the viscous wall layer must be accounted, such that $u_{y1} = U_{yd}$ at $y = 0$. The constant U_{yd} can be found by the wall layer analysis.

The viscous wall layer expansions are

$$\begin{bmatrix} u_x \\ u_y \\ u_z \\ p \end{bmatrix} = \begin{bmatrix} U_{x0}(Y) + \cdots \\ g^{1/2}(\epsilon U_{y0}(Y) + \cdots) \\ g^{1/2}(U_{z0}(Y) + \cdots) \\ g(\epsilon P_0(Y) + \cdots) \end{bmatrix}. \tag{4.12}$$

The no-slip conditions are $U_{x0} = U_{y0} = U'_{y0} = 0$ at $Y = 0$. The leading-order wall-normal component U_{y0} satisfies the equation

$$(i\alpha(\lambda Y - C_1) - \partial_Y^2)U''_{y0} = 0, \tag{4.13}$$

which is the same equation as (2.20). Therefore, the displacement velocity $U_{yd} = \lim_{Y\to\infty} U_{y0} - Y$ is obtained as

$$U_{yd} = -\frac{i^{5/3}\mathrm{Ai}'(\xi_0)}{(\lambda\alpha_0)^{1/3}\kappa(\xi_0)} - \frac{C_1}{\lambda}, \qquad \xi_0 = \frac{i^{7/3}(\lambda\alpha_0)^{1/3}C_1}{\lambda}. \tag{4.14}$$

Multiplying (4.10) by the inhomogeneous equation (4.9) and applying integration by parts, we obtain a dispersion relation similar to (2.25):

$$-\frac{1}{(\lambda\alpha_0)^{1/3}}\frac{i^{5/3}\mathrm{Ai}'(\xi_0)}{\kappa(\xi_0)} + C_1\left(I_1 - \frac{1}{\lambda}\right) + \beta_1 I_2 = 0, \tag{4.15}$$

where

$$I_1 = \int_0^\infty \frac{4\beta_0 u'_{xb} - u''_{xb}}{\lambda^2} e^{-2\beta_0 y}\mathrm{d}y, \qquad I_2 = \int_0^\infty \frac{4u_{xb}u'_{xb} - 2\beta_0 u_{xb}^2}{\lambda^2} e^{-2\beta_0 y}\mathrm{d}y, \tag{4.16}$$

and $\xi_0 = i^{7/3}(\lambda\alpha_0)^{1/3}C_1/\lambda$. For the neutral disturbances, the result simplifies to

$$C_1 = \frac{\lambda s_0}{(\lambda\alpha_0)^{1/3}}, \qquad \beta_1 = \frac{q_0 + s_0(1 - \lambda I_1)}{(\lambda\alpha_0)^{1/3} I_2}, \tag{4.17}$$

where q_0 is the number defined in (2.29), and recall that $s_0 \approx 2.2972$.

So far, we considered a general $u_{xb}(y)$, allowing the results to be applicable to other boundary layer flows. The specific outcomes for the asymptotic suction boundary layer are obtained by setting $u_{xb} = 1 - e^{-y}$ and $\lambda = 1$. For example, the integrals in (4.17) can be solved analytically, resulting in

$$C_1 = \frac{s_0}{\alpha_0^{1/3}}, \qquad \beta_1 = \frac{8\alpha_0^4 + 6\alpha_0^2 + 1}{\alpha_0^{1/3}}\left(q_0 - \frac{4s_0\alpha_0^2}{4\alpha_0^2 + 1}\right). \tag{4.18}$$

For the parameters used in figure 10, the leading-order wavenumbers are obtained as $(\alpha_0, \beta_0) = (0.255, 0.130)$, and we have the approximations

$$\beta = 0.130 - 3.31 g^{-1/6} Re^{-1/3}, \qquad C = 3.62 g^{-1/6} Re^{-1/3}, \tag{4.19}$$

plotted by the blue dash-dotted curves. When the Reynolds number is large, these analytical results provide an excellent approximation for the 'lower branch', which appears as the upper branch in figure 10(*a*). Figure 11 examines the complex phase velocity $C = C_r + iC_i$ near this branch. As noted in § 3, predicting the asymptotic behaviour of the non-neutral modes requires using the full dispersion relation (4.15). As the Reynolds number increases, the numerical data $((\beta - \beta_0)/\epsilon, C/\epsilon)$ converges to the asymptotic result (β_1, C_1). The points where C_i becomes zero correspond to (4.19). Figure 12 compares the eigenfunctions at those neutral points. Once again, we observe clear convergence of the numerical results to the leading-order asymptotic solution.

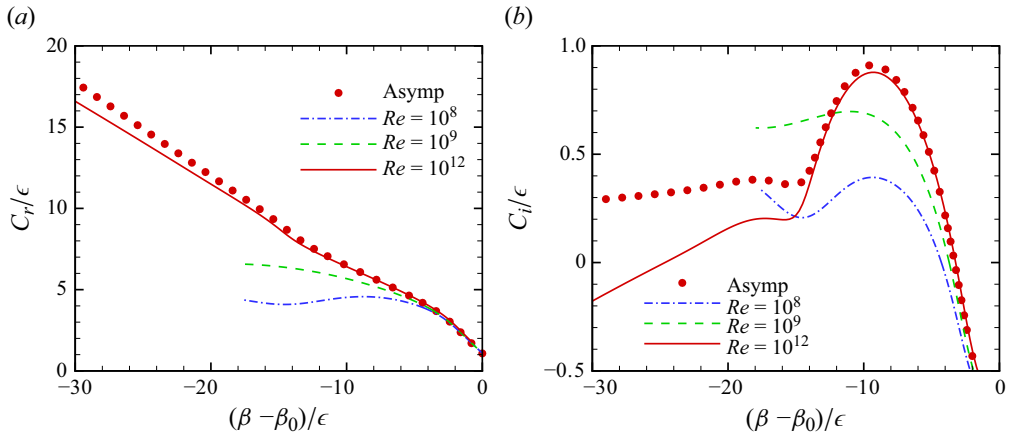

Figure 11. Asymptotic convergence of the phase speed for $\alpha = 0.0036$, $g = 2 \times 10^{-4}$. The curves are computed by (4.6). The points are the asymptotic result (4.15). (*a*) Real part; (*b*) imaginary part.

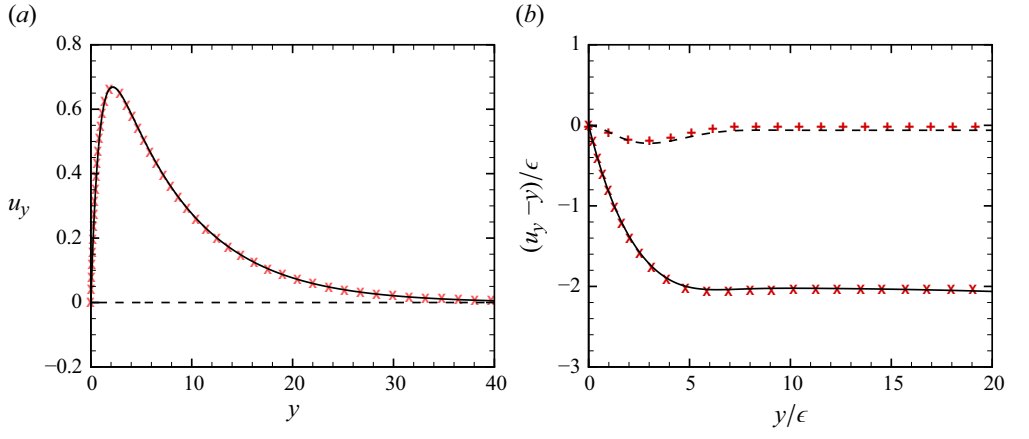

Figure 12. Comparison of the eigenfunctions at the lower-branch neutral point at $(Re, g, \alpha, \beta) = (10^{12}, 2 \times 10^{-4}, 0.0036, 0.130 - 3.30\epsilon)$. The solid and dashed curves are the real and imaginary parts of u_y computed by (4.6). The symbols are the corresponding asymptotic predictions. (*a*) Comparison in the core scaling. The symbols are the leading-order solution u_{y0} found in (4.10). (*b*) Comparison in the wall-layer scaling. The symbols are $U_{y0} - Y$, where U_{y0} is obtained in the same manner as in the derivation of (2.22).

5. Conclusion

By employing matched asymptotic expansion analysis at high Reynolds numbers, we investigated the physical mechanism underlying the D17 mode instability, explaining why it displays distinct properties compared with classical centrifugal instabilities. Our asymptotic predictions closely match numerical results across different flow configurations at finite Reynolds numbers, demonstrating the robustness of our theoretical approach.

Taylor–Couette flow has played a central role throughout the paper, providing a canonical framework for studying the instability mode. In § 2, we examine the narrow gap limit, assuming the inner cylinder to be stationary, which leads to a system that is neutrally

stable according to Rayleigh's stability criterion. We conducted an asymptotic analysis for both the upper and lower branches of the neutral curve. Notably, the structure of the lower branch theory is relatively straightforward and appears to provide a good approximation across a wide range of Reynolds numbers. In § 3, we expanded the lower branch theory to study full Taylor–Couette problem. The D17 mode instabilities occur in both Rayleigh-stable and Rayleigh-unstable scenarios, and this finding is consistent across all radius ratios. In § 4, we introduced a radial cross-flow to the Taylor–Couette flow, forming an asymptotic suction boundary layer near the inner cylinder. This flow configuration serves as a simple prototype for boundary layer flow over a convex wall. The curvature of the wall results in the most unstable mode identified in high-Reynolds-number computations being oblique, which is consistent with the asymptotic analysis.

Our numerical results indicate that the D17 mode instability exists only within a very narrow wavenumber range. This phenomenon, elucidated through asymptotic analysis, likely explains why this mode has remained undetected for so long. The first step in our theoretical study involves determining the inviscid core structure, which reveals that, at leading order, non-trivial modes can only arise around a specific curve in the wavenumber plane. While the unstable region forms around this curve, its width is asymptotically narrow. The next-order analysis shows that this region is bounded by what we refer to as the upper and lower branches of the neutral curve, a terminology derived from the analysis of TS waves (Tollmien (1929); Schlichting (1933) and Lin (1945, 1955)).

To derive the dispersion relation, it is necessary to analyse both the inviscid core and the viscous wall layer near the inner cylinder. The boundary layer structure is similar to, but not identical to, that of TS waves. The D17 mode cannot be identified by considering inviscid theory alone because the instability requires the presence of a viscous boundary layer. However, the viscous wall layer theory alone is insufficient, as the three-dimensional characteristics of the D17 mode are dictated by the inviscid core structure.

The theoretical framework developed here can be extended to more general boundary layers over a convex wall, including those exhibiting spatial growth. These boundary layer problems typically satisfy the condition for the critical layer to appear near the wall, where the tangential component of the base flow vanishes. Noting that the solution (4.10) can also be applied to these general cases, we see that another important requirement – the existence of an inviscid core neutral mode – is guaranteed. For small wall curvature, the properties of the instability at low Reynolds numbers may be indistinguishable from the TS wave in the flat wall case. However, at sufficiently high Reynolds numbers, the D17 mode, characterised by low frequency, short spanwise wavelength, low phase speed and an oblique nature, emerges. In boundary layer transition, it is known that the turbulent transition process depends on external factors. The discovery that even weak wall convexity influences the characteristics of unstable modes may be important for controlling laminar flow over an aeroplane wing, as, depending on the flow conditions, the D17 mode should be accounted for. Furthermore, the fact that the streamwise length scale of the D17 mode is long, but remains shorter than the non-parallel spatial development scale of the base boundary-layer profile, is interesting from the perspective of receptivity theory. The D17 mode has the potential to interact with free stream acoustic or vortical waves and extended surface imperfections, such as roughness, similar to the high-Reynolds-number asymptotic theories by Ruban (1984) and Goldstein (1985).

Finally, we note that this paper primarily focused on cases where the flow is nearly marginally stable according to Rayleigh's criterion. While this assumption simplified the theoretical discussion, the precise range of parameters where the D17 mode occurs remains undetermined. Identifying this range is important for the experimental detection of the D17 mode, which has yet to be observed. The subcritical bifurcation of nonlinear travelling

waves reported by Ayats *et al.* (2020) complicates addressing this issue. An asymptotic approach could facilitate the parameter study of nonlinear states. We speculate that the formulation of the theory may require nonlinear critical layer analysis, similar to that developed by Caillol & Maslowe (2007).

Funding. This research was supported by the Australian Research Council Discovery Project DP230102188. M.D. is also supported by National Natural Science Foundation of China (grant nos 92371104, 11988102), CAS project for Young Scientists in Basic Research (YSBR-087) and Strategic Priority Research Program of Chinese Academy of Sciences (XDB0620102).

Declaration of interests. The authors report no conflict of interest.

Appendix. Operators and functions in the asymptotic analysis of wide-gap Taylor–Couette flow

The operators and functions in (3.5) and (3.6) are defined as

$$\mathscr{L}=\partial_r^2+\left(\frac{3m^2+k_0^2r^2}{r(m^2+k_0^2r^2)}\right)\partial_r+\left(-\frac{m^2}{r^2}-k_0^2+\frac{1}{r^2}+\frac{6k^2m^2+4k_0^4r^2}{m^2(m^2+k_0^2r^2)}\right.$$
$$\left.+\frac{(-3m^4+k_0^2m^2r^2+2k_0^4r^4)\Omega_0'}{m^2r(m^2+k_0^2r^2)\Omega_0}-\frac{\Omega_0''}{\Omega_0}\right), \tag{A1a}$$

$$F_0=\left(\frac{4k_0^2r(3m^2+2k_0^2r^2)\Omega_0+(-3m^4+3k_0^2m^2r^2+4k_0^4r^4)\Omega_0'}{m^2r(m^2+k_0^2r^2)\Omega_0^2}-\frac{\Omega_0''}{\Omega_0^2}\right), \tag{A1b}$$

$$F_1=2k_0\left(\frac{4}{m^2}-1+\frac{2m^2}{(m^2+k_0^2r^2)^2}+\frac{2r[m^4+(m^2+k_0^2r^2)^2]\Omega_0'}{m^2(m^2+k_0^2r^2)^2\Omega_0}\right), \tag{A1c}$$

$$F_2=\frac{4k_0m^2r}{(m^2+k_0^2r^2)^2}, \tag{A1d}$$

$$F_3=\frac{(3m^4-k_0^2m^2r^2-2k_0^4r^4)(\Omega_0'\Omega_1-\Omega_0\Omega_1')}{m^2r(m^2+k_0^2r^2)\Omega_0^2}-\frac{\Omega_1''}{\Omega_0}+\frac{\Omega_1\Omega_0''}{\Omega_0^2}. \tag{A1e}$$

The standard adjoint theory for second-order ordinary differential equations can be used to find the adjoint problem (3.11) with the operator

$$\mathscr{L}^\dagger=\partial_r^2-\left(\frac{3m^2+k_0^2r^2}{r(m^2+k_0^2r^2)}\right)\partial_r+\left(-\frac{m^2}{r^2}-k_0^2+\frac{1}{r^2}+\frac{6k_0^2m^2+4k_0^4r^2}{m^2(m^2+k_0^2r^2)}\right.$$
$$\left.+\frac{(-3m^4+k_0^2m^2r^2+2k_0^4r^4)\Omega_0'}{m^2r(m^2+k_0^2r^2)\Omega_0}-\frac{\Omega_0''}{\Omega_0}\right)-\left(\frac{3m^2+k_0^2r^2}{r(m^2+k_0^2r^2)}\right)'. \tag{A2}$$

References

Abramowitz, M. & Stegun, I.A. 1965 *Handbook of Mathematical Functions with Formulas, Graphs, and Mathematical Tables*. Dover Publications.

Ayats, R., Deguchi, K., Mellibovsky, F. & Meseguer, A. 2020 Fully nonlinear mode competition in magnetised taylor-couette flow. *J. Fluid Mech.* **897**, A14.

Benmalek, A. & Saric, W.S. 1994 Effects of curvature variations on the nonlinear evolution of görtler vortices. *Phys. Fluids* **6**, 3353–3367.

Billant, P. & Gallaire, F. 2005 Generalized Rayleigh criterion for non-axisymmetric centrifugal instabilities. *J. Fluid Mech.* **542** (1), 365–379.

Brockmann, P., Ram, V.I.V., Jakirlić, S. & Hussong, J. 2023 Stability characteristics of the spiral poiseuille flow induced by inner or outer wall rotation. *Intl J. Heat Fluid Flow* **103**, 109172.

Caillol, P. & Maslowe, S.A. 2007 The small vorticity nonlinear critical layer for Kelvin modes on a vortex. *Stud. Appl. Maths* **118** (3), 221–254.

Cowley, S.J. & Smith, F.T. 1985 On the stability of Poiseuille-Couette flow: a bifurcation from infinity. *J. Fluid Mech.* **156**, 83–100.

Deguchi, K. 2016 The rapid-rotation limit of the neutral curve for Taylor–Couette flow. *J. Fluid Mech.* **808**, R2.

Deguchi, K. 2017 Linear instability in Rayleigh-stable Taylor–Couette flow. *Phys. Rev. E* **95** (2), 021102(R).

Drazin, P.G. & Reid, W.H. 1981 *Hydrodynamic Stability*. Cambridge University Press.

Esser, A. & Grossman, S. 1996 Analytic expression for Taylor–Couette stability boundary. *Phys. Fluids* **8** (7), 1814–1819.

Floryan, J.M. 1986 Görtler instability of boundary layers over concave and convex walls. *Phys. Fluids* **29** (8), 2380–2387.

Fransson, J.H.M. & Alfredsson, P.H. 2003 On the disturbance growth in an asymptotic suction boundary layer. *J. Fluid Mech.* **482**, 51–90.

Gallet, B., Doering, C.R. & Spiegel, E.A. 2010 Destabilizing Taylor–Couette flow with suction. *Phys. Fluids* **22** (3), 034105.

Goldstein, M.E. 1985 Scattering of acoustic waves into Tollmien–Schlichting waves by small streamwise variations in surface geometry. *J. Fluid Mech.* **154**, 509–533.

Görtler, H. 1941 Instabilität laminarer grenzschichten an konkaven wänden gegenüber gewissen dreidimensionalen störungen. *Z. Angew. Math. Mech.* **21** (4), 451–459.

Hall, P. 1982 Taylor–Görtler vortices in fuly developed boundary layer flows. *J. Fluid Mech.* **23**, 715–735.

Hall, P. 1983 The linear development of Görtler vortices in growing boundary layers. *J. Fluid Mech.* **130** (1), 41–58.

Hall, P. 1988 The nonlinear development of Görtler vortices in growing boundary layers. *J. Fluid Mech.* **193** (1), 243–266.

Hocking, L.M. 1975 Nonlinear instability of the asymptotic suction velocity profile. *Q. J. Mech. Appl. Maths* **28** (3), 341–353.

Kalburgi, V., Mangalam, S.M. & Dagenhart, J.R. 1988 Görtler instability on an aerofoil: comparison of marching solution with experimental observations. *AGARD CP* **438**, 8.

Karp, M. & Hack, M.J.P. 2018 Transition to turbulence over convex surfaces. *J. Fluid Mech.* **855**, 1208–1237.

Kirillov, O.N. & Mutabazi, I. 2017 Short-wavelength local instabilities of a circular Couette flow with radial temperature gradient. *J. Fluid Mech.* **818**, 319–343.

Lewis, J.W. 1928 An experimental study of the motion of a viscous liquid contained between two coaxial cylinders. *Proc. R. Soc. Lond. A* **117** (777), 388–407.

Lin, C.C. 1945 On the stability of two-dimensional parallel flows. part iii - stability in a viscous fluid. *Q. Appl. Maths* **3** (4), 277–301.

Lin, C.C. 1955 *The Theory of Hydrodynamic Stability*. Cambridge University Press.

Meseguer, A. 2002 Energy transient growth in the Taylor–Couette problem. *Phys. Fluids* **14** (5), 1655–1660.

Miles, J.W. 1960 The hydrodynamic stability of a thin film of liquid in uniform shearing motion. *J. Fluid Mech.* **8** (4), 593–610.

Milinazzo, F.A. & Saffman, P.G. 1985 Finite-amplitude steady waves in plane viscous shear flows. *J. Fluid Mech.* **160**, 281–295.

Rayleigh, Lord 1917 On the dynamics of revolving fluids. *Proc. R. Soc. Lond. A* **93** (648), 148–154.

Romanov, V.A. 1973 Stability of hydrodynamic Couette flow. *Funct. Anal. Applics* **7** (2), 137–146.

Ruban, A.I. 1984 On Tollmien schlichting wave generation by sound (in russian), (Translation in. *Izv. Akad. Nauk SSSR Mekh. Zhidk. Gaza Fluid Dyn.* **5–19**, 44-709–752-716.

Saric, W.S. 1994 Görtler vortices. *Annu. Rev. Fluid Mech.* **26** (1), 379–409.

SCHLICHTING, H. 1933 Laminare strahlenausbreitung. *Z. Angew Math. Mech.* **13** (4), 260–263.
SYNGE, J.L. 1938 On the stability of a viscous liquid between rotating coaxial cylinders. *Proc. R. Soc. Lond. A* **167** (929), 250–256.
TAYLOR, G.I. 1923 Stability of a viscous liquid contained between two rotating cylinders. *Phil. Trans. R. Soc. Lond. A* **223**, 289–343,
TOLLMIEN, W. 1929 Uber die entstehung der turbulenz. *Nachr. Ges. Wiss. Gottingen Math-Pyhs. Kl* **II**, 21–44.